Supporting Information for "Atlantic ocean heat transport enabled by Indo-Pacific heat uptake and mixing"

Ryan M. Holmes[1,2], Jan D. Zika[2], Raffaele Ferrari[3], Andrew F. Thompson[4],

Emily R. Newsom[5], and Matthew H. England[1]

[1]Climate Change Research Centre and the ARC Centre of Excellence for Climate Extremes, University of New South Wales, Sydney, NSW, Australia

[2]School of Mathematics and Statistics, University of New South Wales, Sydney, NSW, Australia

[3]Department of Earth, Atmosphere and Planetary Sciences, Massachusetts Institute of Technology, Cambridge, Massachusetts, U.S.A.

[4]Environmental Science and Engineering, California Institute of Technology, Pasadena, California, U.S.A.

[5]Department of Physics, University of Oxford, Oxford, United Kingdom

Contents of this file

Introduction

Corresponding author: R. M. Holmes, Climate Change Research Centre, University of New South Wales, Sydney, NSW, Australia (ryan.holmes@unsw.edu.au)

The supporting information contains a number of supplementary figures referred to in the main article as well as brief discussions of the model configuration and numerical details of the diagnostic calculations (text S1), the contribution of various parameterized mixing processes to the total mixing (text S2), a discussion of heat transport in the presence of a net meridional volume transport through Bering Strait (text S3) and a comparison of the model meridional heat transport to observational products (text S4).

Text S1: Model details and the numerical diagnostic calculations

The model configuration used is the MOM025 Control simulation of HZE19. Vertical mixing, captured within the term $\mathcal{M}$ in Eq. 10, is parameterized using the K-profile parameterization (Large, McWilliams, & Doney, 1994), a bottom-enhanced internal tide mixing scheme (Simmons, Jayne, Laurent, & Weaver, 2004) and a background vertical diffusivity. The MOM025 Control background diffusivity κ_B is latitude dependent being $10^{-5}\mathrm{m}^2\mathrm{s}^{-1}$ poleward of 15° latitude and reducing linearly to $10^{-6}\mathrm{m}^2\mathrm{s}^{-1}$ within 5° of the Equator. MOM025 Control was initialized from the end of a similar 500 year simulation with no background diffusivity (the $\kappa_B = 0$ case considered by HZE19) and then run for an additional 111 years to equilibrate to the change in κ_B. Analysis comes from the last 10 years.

We use the same methods to calculate the diathermal fluxes as in HZE19. However, here the latitudinally-resolved heat budget also includes lateral heat transports, which were zero by definition in the globally-integrated budget of HZE19. The stream function Ψ is obtained by accumulating the volume transport within 0.5°C temperature bins online at each grid point, as for the other diagnostics. We tested several methods of calculating

the internal heat content transport $\mathcal{A}_I$. The best method was found to be subtracting the external heat transport component $\mathcal{A}_E$ [Eq. 7] from the total meridional heat transport $\mathcal{A}(\phi, \Theta, t)$ calculated by accumulating the meridional heat flux relative to 0°C within each temperature bin online. Other methods, such as calculating $\mathcal{A}_I$ by directly integrating the stream function [via Eq. 8] yielded similar results, with a higher level of noise.

MOM025 Control does not include a mesoscale eddy parameterization or explicit isopycnal or lateral diffusion. The suppression of large lateral tracer gradients is thus achieved by the multi-dimensional piece-wise parabolic tracer advection scheme (Colella and Woodward (1984), with a monotonicity-preserving flux limiter following Suresh and Huynh (1997)). As in HZE19 the across-isotherm diffusive heat flux associated with the numerical advection scheme (referred to as numerical mixing) is calculated by residual. Here it is included in the mixing term $\mathcal{M}$ (see supplementary text S2).

The model configuration also includes a parameterization for submesoscale restratification (Fox-Kemper, Ferrari, & Hallberg, 2008). This parameterization is implemented through skew-diffusion (Griffies, 1998), and therefore is not associated with any explicit volume circulation (i.e. it does not alter Ψ). Hence, its influence on the internal heat content budget is through its meridional heat flux included in $\mathcal{A}_D$ as part of $\mathcal{A}_I$ in Eq. 8. While skew-diffusion should not result in any across-isotherm fluxes of heat, its numerical implementation may induce some such fluxes, which are included in the numerical mixing flux across isotherms.

Text S2: The processes contributing to mixing

The diathermal heat transport arising from mixing contains contributions from a number of explicitly-parameterized vertical mixing processes (Fig. S2a-c,e,f) and numerical mixing (Fig. S2d). The strongest vertical mixing fluxes are focused very close to the Equator between 15°C and 28°C and are associated with shear instability (Fig. S2c) in the eastern equatorial Pacific cold tongue (e.g. see Fig. 4c of HZE19). Background mixing is significant across most of the temperature-latitude plane, in particular in the interior subtropical regions, driving most of the diathermal heat flux in those regions responsible for the downward slope in the heat function (e.g. compare Fig. 2d and Fig. S2b between 15°C and 20°C in the latitude range 10°-30° in both hemispheres). Background mixing is also strong around the surface outcrop regions at all latitudes. The sensitivity of the diathermal heat transport to the background diffusivity is examined in HZE19 (also see Hieronymus, Nycander, Nilsson, Döös, & Hallberg, 2019). Boundary layer mixing is relatively uniformly distributed with latitude and focused around the surface outcrops (Fig. S2e), although there is also a peak around the Equator associated with the eastern equatorial Pacific cold tongue (e.g. see Fig. 4d of HZE19). Mixing associated with the bottom-intensified tidal mixing scheme of Simmons et al. (2004) is relatively uniform with temperature and focused in the tropics and mid-latitudes, although there are also peaks in the high northern latitudes (Fig. S2f).

Numerical mixing (see text S1) also makes a significant contribution to the diathermal heat transport (Fig. S2d). As discussed in more detail in HZE19, the large contribution of numerical mixing arises because sources of explicit mixing have been minimized in this model configuration (e.g. the lack of any explicit lateral mixing) in order to minimize

the overall levels of mixing. Numerical mixing drives down-gradient heat fluxes that are peaked in the equatorial regions at temperatures above ~ 15°C and along the mid-latitude outcrop regions. The peak near the equator is likely associated with the strong vertical temperature gradients and vertical velocity variability in that region. The numerical mixing at higher latitudes near the surface outcrops, which in many cases is stronger than the explicit vertical mixing, may be associated with along-isopycnal eddy stirring and the subsequent dissipation of along-isopycnal temperature gradients that is not explicitly parameterized. The structure and causes of numerical mixing will be examined in more detail in a forthcoming article.

Text S3: Heat transport in the presence of a net meridional volume transport through Bering Strait

The presence of a net lateral volume transport (through a passage such as the Bering Strait) introduces some ambiguity into the meaning and value of the associated heat transport. In MOM025 Control there is a mean transport of $\Psi_{BS}(\Theta^{max}) = +1.03$Sv through Bering Strait, where the maximum SST is $\Theta^{max} = 10.5$°C. The associated total internal heat content transport below Θ^{max} is southward (due to the negative sign in Eq. 8) with value -0.04PW, in the opposite direction to the volume transport. This southward heat transport arises because, as defined in Eq. 8, the internal heat content transport evaluated at some value of Θ greater than or equal to Θ^{max} inherently assumes that water returns back through the Bering Strait, closing the circulation, at temperature Θ. This also implies that the magnitude of the internal heat content transport continues to increase when evaluated at temperatures Θ greater than Θ^{max} (i.e. $\mathcal{J}_\phi = \frac{\partial \mathcal{A}_I}{\partial \Theta}$ is non-

zero even at temperatures greater than Θ^{max}). As the volume flux through Bering Strait is largely closed by passage through the Indo-Pacific and Atlantic basins via the Southern Ocean (while also being modified by surface volume fluxes), this heat flux ambiguity also affects the heat budgets of these basins.

For the purposes of the schematic in Fig. 4 the heat budget of each layer is constructed between the cooler isotherm (e.g. 15°C for the 15° to 20°C layer) and the colder of either the warm isotherm or the maximum SST Θ^{max} at each latitude (upper thin dotted line in Fig. 2). The temperature of the upper boundary of the layer thus varies with latitude, meaning that to close the heat budget of the layer the meridional component of the heat transport, $\frac{\partial \mathcal{A}_I}{\partial \Theta}(\phi, \Theta^{max}, t)$, exiting this upper boundary must be taken into account. For the purposes of Fig. 4, this heat transport is included as part of the surface forcing term. The changes to Fig. 4 resulting from this procedure (compared to using the upper isotherm Θ even when it is warmer than Θ^{max}) are minimal and are restricted to the transport through Bering Strait (as discussed next) and some small changes to the high-latitude surface heat fluxes and the southward transport above 20°C across 34°S out of the Indo-Pacific.

A bound for the effective magnitude of the heat transport through the Bering Strait, corresponding to a bound for the ambiguity on the Indo-Pacific and Atlantic heat budgets, can be constructed by matching the Bering Strait volume and heat transport with estimates of the return transport via the Southern Ocean (e.g. see Vranes, Gordon, & Ffield, 2002, who discuss the Indonesian Throughflow heat transport). The net heat transport

associated with the Bering Strait volume transport Ψ_{BS} is,

$$MHT_{BS} = \rho_0 C_p \left(\overline{\Theta}_{BS} - \overline{\Theta}_{SO}\right) \Psi_{BS}(\Theta^{max}), \tag{1}$$

where $\overline{\Theta}_{BS}$ and $\overline{\Theta}_{SO}$ are transport weighted temperatures through the Bering Strait and the return pathway via the Southern Ocean. Using the MOM025 Control Bering Strait mass transport ($\Psi_{BS} = +1.03$Sv) and heat transport relative to 0°C ($\mathcal{A}_{BS} = +0.003$PW), we find that $\overline{\Theta}_{BS} = \mathcal{A}_{BS}/\left(\rho_0 C_p \Psi_{BS}\right) = 0.76$°C. However, $\overline{\Theta}_{SO}$ is uncertain, as it depends on which portion of the heat transport via the return pathway through the Southern Ocean is matched to Ψ. Considering values of $\overline{\Theta}_{SO}$ in the large range −2°C to 20°C yields a range for MHT_{BS} of between −0.08 and +0.01PW. Observations suggest that this heat transport does not exceed 0.02PW, using a reference temperature of −1.9°C (Woodgate, 2018). These values are less than the minimum transport of 0.1PW shown in Fig. 4, and thus the ambiguity is relatively small. However, for passages where the net volume transport is much larger the associated ambiguity is also much larger. For this reason we do not examine in detail the heat transports through Drake Passage or the Indonesian Throughflow.

Text S4: Heat transport comparison with observational estimates and a fine resolution model

The MOM025 Control meridional heat transport (solid lines in Fig. S3) compares favorably with both direct and indirect observational estimates (dashed lines and markers with error bars in Fig. S3, Ganachaud & Wunsch, 2003; Trenberth, Zhang, Fasullo, & Cheng, 2019). The Atlantic heat transport in particular is well represented (red lines in Fig. S3). The southward heat transport in the Southern Hemisphere Indo-Pacific is weaker than

observations suggest. This appears to be a common problem with many global ocean models, and it remains unclear whether this problem is linked to model biases or observational errors (e.g. Griffies et al., 2009; Trenberth & Caron, 2001; Valdivieso et al., 2017). A similar MOM-SIS configuration with a finer horizontal resolution of 1/10° (MOM01, which also has 75 vertical levels instead of 50, and no background vertical diffusivity) has similar heat transport in the Indo-Pacific but significantly weaker transport in the Atlantic (thin solid lines in Fig. S3), which is linked to a weaker NADW circulation (not shown). Hence we have chosen to focus on MOM025 Control in this study. Nevertheless, a similar analysis to that performed in the main article applied to MOM01 shows that the contribution of Indo-Pacific heat uptake and mixing to Atlantic meridional heat transport remains similar. 52% (0.28PW) of the 0.54PW of northward heat transport across 50°N in the Atlantic in MOM01 is supplied across 34°S ultimately from temperatures above 20°C in the Indo-Pacific, while 0.19PW is supplied through mixing across the 15°C isotherm in the Atlantic. Thus our qualitative conclusions are robust to the differences between MOM01 and MOM025 Control.

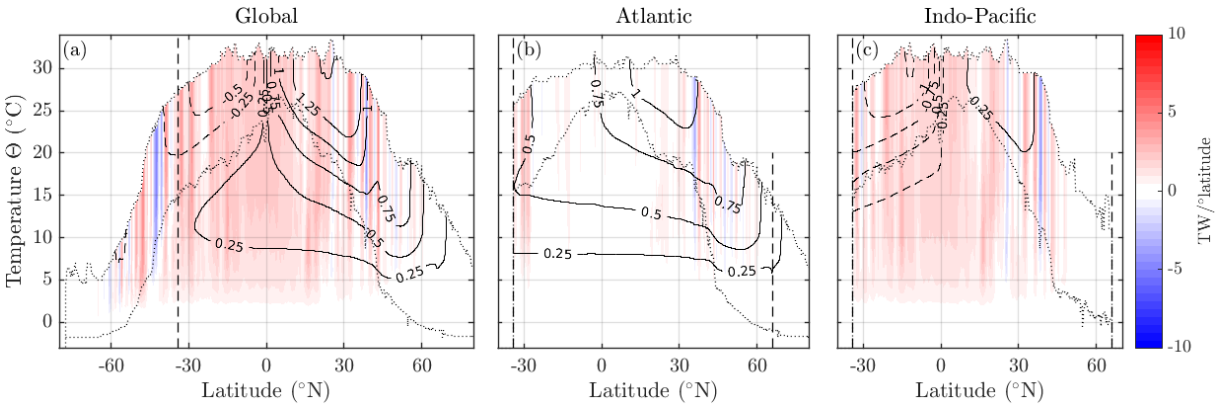

Figure S1. MOM025 Control (a) global, (b) Atlantic and (c) Indo-Pacific internal heat content tendency $[\partial/\partial t\,(\partial\mathcal{H}_I/\partial\phi)$, TW/° latitude]. At each temperature the color corresponds to the net flux of heat into all fluid colder than that temperature within each latitude band. The heat function $\mathcal{A}_I$ is shown in thin black 0.25PW contours for each basin, with the solid (dashed) contours indicating positive (negative) values. The thin dotted lines mark the minimum and maximum SST at each latitude at all zonal locations and seasons within each basin.

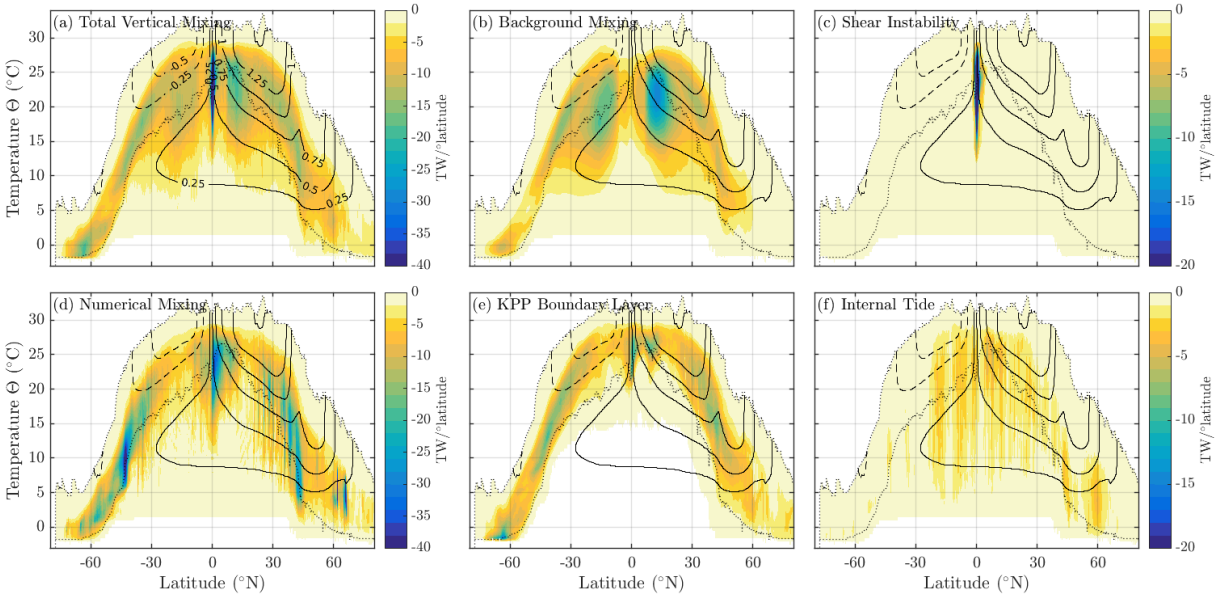

Figure S2. The MOM025 Control global diathermal heat transport due to mixing ($\partial\mathcal{M}/\partial\phi$ in Eq. (13), Fig. 3d) decomposed into its components due to (a) explicitly parameterized total vertical mixing and (d) numerical mixing. The explicitly parameterized vertical mixing (panel a) includes components due to (b) background mixing, (c) interior shear instability, (e) boundary layer mixing and (f) internal tide mixing and several other small processes (e.g. double-diffusion, not shown). The heat function is shown in black 0.25PW contours. The thin dotted lines mark the zonal minimum and maximum SST at each latitude at all zonal locations and seasons.

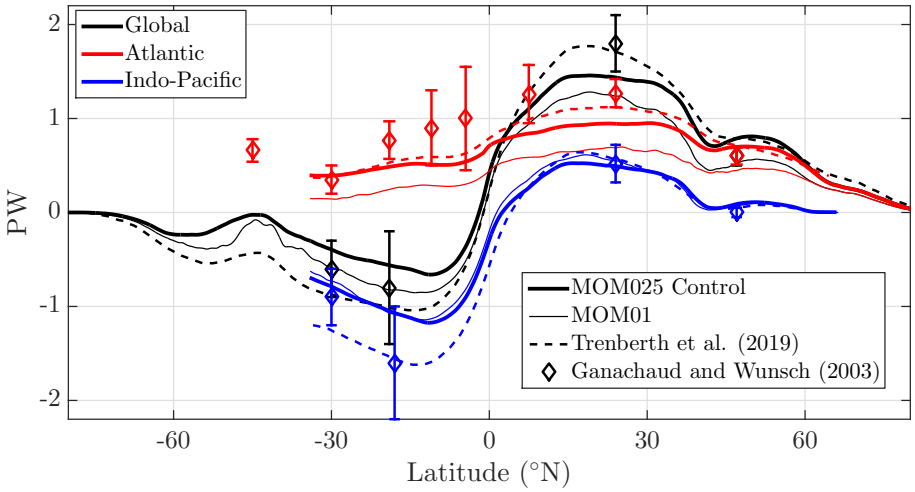

Figure S3. Total meridional heat transport in MOM025 Control (thick solid lines), MOM01 (thin solid lines) and from observational estimates from a World Ocean Circulation Experiment inversion (Ganachaud & Wunsch, 2003, markers with error bars) and from reanalysis data (Trenberth et al., 2019, dashed lines). Note that here, as opposed to in Fig. 2 of the main article, all curves represent the total heat transport relative to a reference temperature of 0°C.